Time-Varying Rician K-factor in Measured Vehicular Channels at cmWave and mmWave Bands

Faruk Pasic*, Markus Hofer†, Thomas Zemen†, Andreas F. Molisch‡ and Christoph F. Mecklenbräuker*

*Institute of Telecommunications, TU Wien, Vienna, Austria

†AIT Austrian Institute of Technology, Vienna, Austria

‡Ming Hsieh Department of Electrical and Computer Engineering, University of Southern California, Los Angeles, USA

faruk.pasic@tuwien.ac.at

Abstract—**Future vehicular communication systems will integrate millimeter wave (mmWave) technology to enhance data transmission rates. To investigate the propagation effects and small-scale fading differences between mmWave and conventional centimeter wave (cmWave) bands, multi-band channel measurements have to be conducted. One key parameter to characterize small-scale fading is the Rician K-factor. In this paper, we analyze the time-varying K-factor of vehicle-to-infrastructure (V2I) channels across multiple frequency bands, measured in an urban street environment. Specifically, we investigate three frequency bands with center frequencies of 3.2 GHz, 34.3 GHz and 62.35 GHz using measurement data with 155.5 MHz bandwidth and a sounding repetition rate of 31.25 μs. Furthermore, we analyze the relationship between K-factor and root-mean-square (RMS) delay spread. We show that the Ricean K-factor is similar at different frequency bands and that is correlated with the RMS delay spread.**

Index Terms—**multi-band, cmWave, mmWave, channel measurements, vehicle-to-infrastructure, K-factor, RMS delay spread**

I. Introduction

Due to the high utilization of conventional centimeter wave (cmWave) (sub-6 GHz) bands, there is a bandwidth shortage that results in lower data transmission rates. Conversely, millimeter wave (mmWave) bands (24 GHz – 300 GHz) [1] offer larger bandwidth communication channels, which enables achieving higher data rates [2]. Therefore, mmWave technology is attracting significant attention for future vehicular communication systems.

To understand how propagation and small-scale effects differ between cmWave and mmWave bands, comparative measurements across these frequency bands are necessary [3]. Numerous studies in the literature have analyzed multi-band propagation in vehicular [4]–[9], indoor [10]–[13] and cellular [14] scenarios. These studies examine various channel parameters, such as path loss, blockage loss, angular spread, root-mean-square (RMS) delay and Doppler spread.

One key parameter to characterize small-scale fading is the Rician K-factor, which defines the ratio of deterministic to stochastic multi-path components [15]. Understanding the K-factor is crucial for designing transmission and reception techniques aimed at mitigating the small-scale fading effects [16], [17]. Given the significant differences in wavelength between cmWave and mmWave bands, it is essential to examine how the K-factor varies across these frequency bands. Only one measurement-based multi-band analysis of the K-factor can be found in the literature, specifically in [14]. In [14], the authors examine the K-factor in urban micro and outdoor-to-indoor scenarios, with configurations where either a single antenna or both the transmit and receive antennas are positioned at elevated heights within the building. To the best of our knowledge, no other research has analyzed the K-factor across multiple bands. Moreover, there is no analysis of the K-factor across multiple bands in vehicular scenarios, where the transmit and receive antennas are placed at average car heights.

Contribution: In this paper, we present a comparative analysis of the time-varying Rician K-factor between the cmWave and mmWave frequency bands based on multi-band vehicle-to-infrastructure (V2I) channel measurements. Specifically, our measurements have been conducted simultaneously at center frequencies of 3.2 GHz, 34.3 GHz and 62.35 GHz in an urban street environment. Furthermore, we investigate the correlation between the K-factor and the RMS delay spread.

Organization: The remainder of the paper is organized as follows. Section II provides a detailed description of the multi-band channel measurements. In Section III, we explain the evaluation and post-processing of the measured data. Section IV discusses the results, focusing on the Rician K-factor and RMS delay spread. Finally, Section V concludes the paper.

II. Measurement Data Description

For the analysis of the K-factor in this paper, we use V2I multi-band channel measurements described in detail in [6]. The channel measurements are conducted simultaneously at carrier frequencies of 3.2 GHz, 34.3 GHz and 62.35 GHz, with a measurement bandwidth of 155.5 MHz for each frequency band. At the transmit side, we use custom-built omnidirectional monopole antennas mounted on a car rooftop for all three frequency bands, as shown in Fig. 1. The transmit antennas are arranged in a straight line along the direction of travel, with the 62.35 GHz antenna positioned at the front, followed by the 34.3 GHz and the 3.2 GHz antenna. The antennas are mounted at a uniform height to ensure that all ground planes are at the same level. At the receive side, we use directional antennas with similar radiation patterns mounted on a tripod, as shown in Fig. 1. Specifically, we
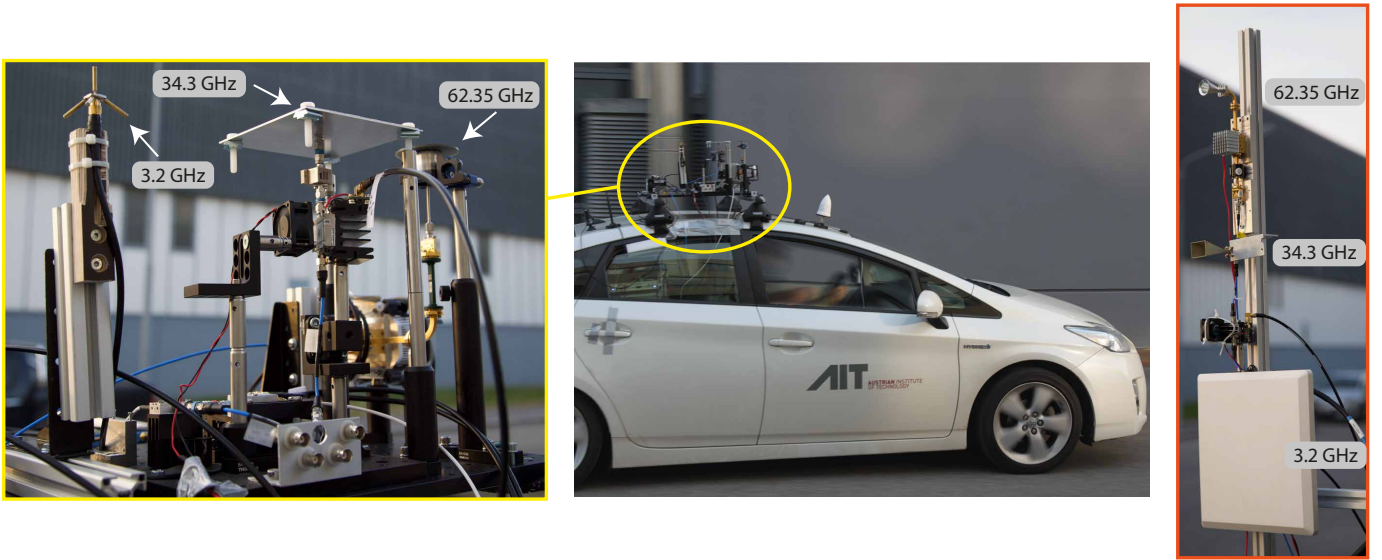
Fig. 1. Transmit antennas (left) are mounted on the roof of a car (middle). Receive antennas (right) are mounted on a pole of a tripod.
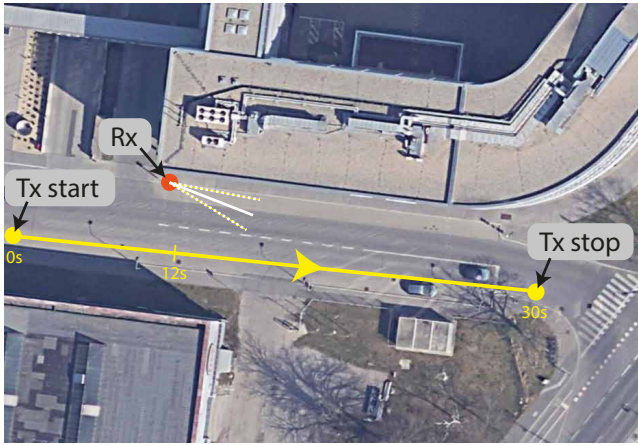

Fig. 2. A car approaches an intersection and stops. The directional receive antennas are pointed towards the intersection.

Parameter	Value
Carrier Frequency f_c	3.2, 34.3, 62.35 GHz
Number of Subcarriers K	311
Subcarrier Spacing $\triangle f$	500 kHz
Bandwidth B	155.5 MHz
Symbol Duration t_s	2 µs
Symbols per Snapshot N_{sym}	5
Interval Between Snapshots t_R	31.25 µs
Snapshot Duration t_{snap}	10 µs
Number of Snapshots N	960 000
Measurement Duration t_m	30 s
Max. Relative Velocity v_{max}	1500, 140, 77 m/s

use a patch array antenna for 3.2 GHz with a 17° half-power beamwidth (HPBW) and 18 dBi gain, a Fairview SMH128KR-20 horn antenna for 34.3 GHz with an 18.3° HPBW and 20 dBi gain and a Pasternack PE-9881-20 conical horn antenna for 62.35 GHz with an 18° HPBW and 20 dBi gain. The 3.2 GHz patch antenna is mounted 159 cm above the ground level. The 34.2 GHz and 62.35 GHz horn antennas are mounted 34.8 cm and 64 cm above the 3.2 GHz patch antenna, respectively.

Using this setup, we conduct channel measurements in an industrial area in Vienna, as illustrated in Fig. 2. The vehicle (Toyota Prius), equipped with the transmit antennas, moves towards the receiver. The receiver is mounted on a tripod on the left side of the street and remains static throughout the measurement campaign. After passing the receiver, the transmit vehicle approaches a "T"-intersection with traffic lights and stops. The receive antennas are oriented towards

this stop point at the intersection.

For all frequency bands, we follow the same measurement procedure. We transmit a sequence of complex baseband orthogonal frequency-division multiplexing (OFDM) symbols with a low Crest factor [18] as the channel-sounding signal. The measurement parameters are provided in Tab. I. At the receiver, the measurement sequence is divided into 960 000 snapshots, each containing 5 symbols. The first OFDM symbol of each snapshot is used as a cyclic prefix and then discarded. The remaining 4 symbols are averaged to improve the signal-to-noise ratio (SNR). After OFDM processing, we estimate the wireless channel for all subcarriers using least-square estimation given by [19]

$$\mathrm{H}[k,n] = \frac{\mathrm{Y}[k,n]}{\mathrm{X}[k]\mathrm{H}^{\mathrm{RF}}[k]}, \tag{1}$$

where k is the subcarrier index, n is the snapshot index,

$H^{RF}[k]$ represents the radio frequency (RF) chain calibration function, $X[k]$ is the known transmit complex amplitude and $Y[k, n]$ denotes the received complex amplitude. Calibration is performed by directly connecting the transmitter with the receiver via attenuators and measuring $H^{RF}[k]$. Finally, we have the time-variant channel transfer function (CTF) $H[k, n]$, with $k \in \{0, \ldots, K-1\}$ subcarriers and $n \in \{0, \ldots, N-1\}$ time symbols. For simplicity of notation, we omit the index for the frequency band.

III. MEASUREMENT EVALUATION

For each frequency band, we assume the channel to be locally stationary within a window of $T_{\text{stat}} = 100\,\text{ms}$ of motion and over the entire frequency range, without further justification. The chosen stationarity time-window corresponds to $N_{\text{stat}} = 3200$ time symbols per stationarity region, resulting in $L_{\text{stat}} = N/N_{\text{stat}} = 300$ stationarity regions. Hence, we have the time-variant CTF $H^{(i)}[k, n]$, with $k \in \{0, \ldots, K-1\}$ subcarriers, $n \in \{0, \ldots, N_{\text{stat}} - 1\}$ time symbols per stationarity region and $i \in \{0, \ldots, L_{\text{stat}} - 1\}$ stationarity regions. We first convert the time-variant CTF $H^{(i)}[k, n]$ to the delay domain $H^{(i)}[\tau, n]$, using the inverse discrete Fourier transform (IDFT). The dynamic range (DR) is defined as the difference between the maximum power of $H^{(i)}[\tau, n]$ and a level 6 dB above the noise floor. The noise floor is determined by the median, following the procedure described in [20]. To ensure a fair comparison, we choose the DR to be the smallest one of the three bands. We set values smaller than the DR to be zero. Finally, we transform the time-variant channel impulse response (CIR) $H^{(i)}[\tau, n]$ back to the frequency domain $H^{(i)}[k, n]$, using the discrete Fourier transform (DFT).

A. K-factor Estimation

To estimate the K-factor, we use the technique introduced in [21], based on the method of moments (MoM) [22]. First, we calculate the power of the time-variant channel $H^{(i)}[k, n]$ as

$$P_{\text{H}}^{(i)}[k, n] = \left| H^{(i)}[k, n] \right|^2. \tag{2}$$

The first moment, or the average power of the time-variant channel, is given as

$$\overline{P}_{\text{H}}^{(i)} = \frac{1}{K N_{\text{stat}}} \sum_{k=0}^{K-1} \sum_{n=0}^{N_{\text{stat}}-1} P_{\text{H}}^{(i)}[k, n] \tag{3}$$

and the second moment of interest is the RMS fluctuation of $P_{\text{H}}^{(i)}[k, n]$ about $\overline{P}_{\text{H}}^{(i)}$ given by

$$v_{\text{P}}^{(i)} = \sqrt{\frac{1}{K N_{\text{stat}}} \sum_{k=0}^{K-1} \sum_{n=0}^{N_{\text{stat}}-1} \left(P_{\text{H}}^{(i)}[k, n] - \overline{P}_{\text{H}}^{(i)} \right)^2}. \tag{4}$$

Next, the power of the constant channel term is computed as

$$\left| V^{(i)} \right|^2 = \sqrt{\left(\overline{P}_{\text{H}}^{(i)} \right)^2 - \left(v_{\text{P}}^{(i)} \right)^2} \tag{5}$$

and the power of the fluctuating channel term is given by

$$\left(\sigma^{(i)} \right)^2 = \overline{P}_{\text{H}}^{(i)} - \left| V^{(i)} \right|^2. \tag{6}$$

Finally, the estimated K-factor for the i-th stationarity region is given by the ratio of the constant to the fluctuating channel term, expressed as

$$K^{(i)} = \frac{\left| V^{(i)} \right|^2}{\left(\sigma^{(i)} \right)^2}. \tag{7}$$

B. RMS Delay Spread Estimation

To estimate the RMS delay spread, we use the approach from [23]. Using the time-variant CTF $H^{(i)}[k, n]$, we first estimate the local scattering function (LSF) given as

$$\mathcal{C}^{(i)}[\tau, \nu] = \frac{1}{IJ} \sum_{w=0}^{IJ-1} \left| \mathcal{H}_w^{(i)}[\tau, \nu] \right|^2 \tag{8}$$

with the Doppler index $\nu \in \{-N_{\text{stat}}/2, \ldots, N_{\text{stat}}/2 - 1\}$ and the delay index $\tau \in \{0, \ldots, K-1\}$. The windowed frequency response is

$$\mathcal{H}_w^{(i)}[\tau, \nu] = \sum_{k=-K/2}^{K/2} \sum_{n=-N_{\text{stat}}/2}^{N_{\text{stat}}/2-1} H[k, n + iN_{\text{stat}}]$$
$$\cdot G_w[k, n] e^{-j2\pi(\nu n - \tau k)}, \tag{9}$$

where the tapers $G_w[k, n]$ are two-dimensional discrete prolate spheroidal sequences as shown in detail in [23], [24]. The number of tapers in the time and frequency domain is set to $I = 2$ and $J = 1$ [6], respectively. We calculate the power delay profile (PDP) as the expectation of the LSF over the Doppler domain, given by

$$\mathcal{P}^{(i)}[\tau] = \frac{1}{N_{\text{stat}}} \sum_{\nu=-N_{\text{stat}}/2}^{N_{\text{stat}}/2-1} \mathcal{C}^{(i)}[\tau, \nu]. \tag{10}$$

Further, we calculate the RMS delay spread $\sigma_\tau^{(i)}$ as second-order moment of $\mathcal{P}^{(i)}[\tau]$ given by

$$\sigma_\tau^{(i)} = \sqrt{\frac{\sum_{\forall \tau} \tau^2 \mathcal{P}^{(i)}[\tau]}{\sum_{\forall \tau} \mathcal{P}^{(i)}[\tau]} - \left(\frac{\sum_{\forall \tau} \tau \mathcal{P}^{(i)}[\tau]}{\sum_{\forall \tau} \mathcal{P}^{(i)}[\tau]} \right)^2}. \tag{11}$$

Finally, we compute the correlation coefficient between the K-factor $K^{(i)}$ and the RMS delay spread $\sigma_\tau^{(i)}$ given by

$$\rho = \frac{\sum_{i=0}^{L_{\text{stat}}-1} \left(K^{(i)} - \overline{K} \right) \left(\sigma_\tau^{(i)} - \overline{\sigma_\tau} \right)}{\sqrt{\sum_{i=0}^{L_{\text{stat}}-1} \left(K^{(i)} - \overline{K} \right)^2} \sqrt{\sum_{i=0}^{L_{\text{stat}}-1} \left(\sigma_\tau^{(i)} - \overline{\sigma_\tau} \right)^2}}, \tag{12}$$

where $\overline{K} = \frac{1}{L_{\text{stat}}} \sum_{i=0}^{L_{\text{stat}}-1} K^{(i)}$ and $\overline{\sigma_\tau} = \frac{1}{L_{\text{stat}}} \sum_{i=0}^{L_{\text{stat}}-1} \sigma_\tau^{(i)}$ represent the mean values of the K-factor and the RMS delay spread, respectively.

IV. RESULTS

Here, we present the results obtained using the procedure outlined in Section III. Although the entire measurement spans 30 s, we focus on a specific time interval. During the first 12 s, the transmit car is located behind the receiver, whose antennas
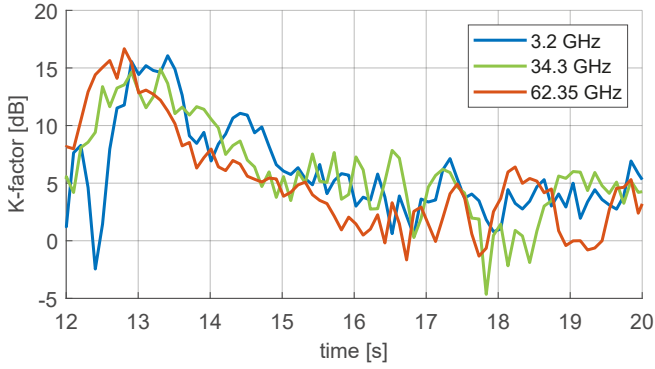
Fig. 3. The K-factor varies over time and exhibits a similar temporal trend for both cmWave and mmWave bands.
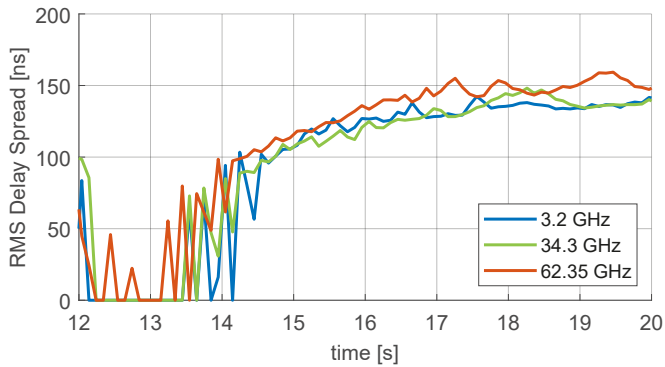

Fig. 5. In the three frequency bands, the CDF of the K factor shows similar behavior.

Fig. 4. The RMS delay spread varies over time and shows a clear relationship to the K-factor.

Fig. 6. The CDF of the RMS delay spread across cmWave and mmWave bands looks similar, with only minor variations.

are oriented in the opposite direction. As a result, the line-of-sight (LOS) component is negligible, making the estimation of the time-varying K-factor irrelevant in this period. From 12 to 20 s, the transmit car passes the receiver and moves towards the intersection. At this point, the transmit car moves within the main lobe of the receive antennas. Finally, between 20 and 30 s, the transmit car remains static at the intersection, leading to a loss of time variability in the channel. Therefore, our analysis focuses on the 12 to 20 s time span, where the most relevant channel dynamics occur.

We plot in Fig. 3 the time evolution of the K-factor for three different frequency bands. The results show that the K-factor varies over time and exhibits a similar temporal trend across all three frequency bands. As the transmit car passes the receiver and enters the main lobe of the receive antennas (between 12 and 13 s), the K-factor increases significantly. In this period, the free-space LOS component dominates, causing the K-factor to reach values around 15 dB. However, as the transmit car moves further away from the receiver (from 13 to 20 s), the K-factor decreases. In this case, there are more significant diffuse components present in the received signal, leading to a reduction in the K-factor, which drops mainly to values between 0 and 5 dB.

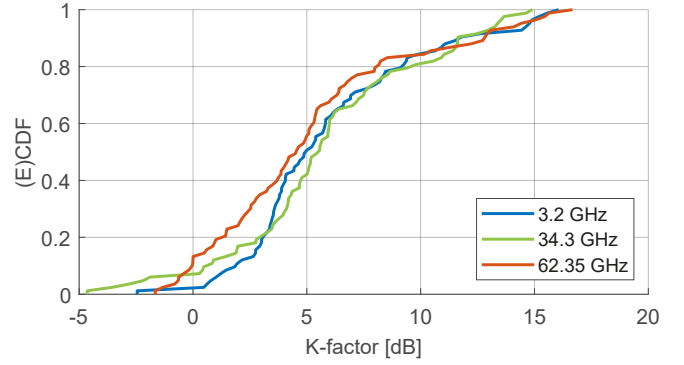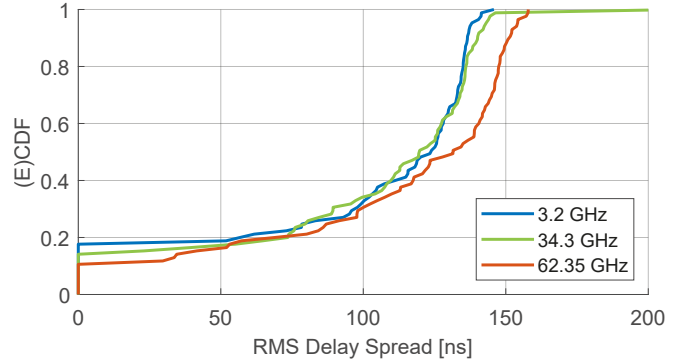In Fig. 4, we show the time evolution of the RMS delay spread for three different bands. The RMS delay spread varies over time, exhibiting a similar trend across different bands. Between 12 and 13 s, as the transmit car approaches the main lobe of the receive antennas, the RMS delay spread drops to around zero. As the car moves away from the receiver, the RMS delay spread increases to approximately 150 ns. This demonstrates a clear relationship between the K-factor and the RMS delay spread: when the K-factor decreases, the RMS delay spread increases, and vice versa.

In Fig. 5 and Fig. 6, we plot the CDF of the K-factor and the RMS delay spread. The obtained mean and standard deviation values are summarized in Tab. II. We observe that the obtained mean and standard deviation values at the three frequency bands are comparable although they do not have the same numerical value.

The estimated correlation coefficient ρ between the K-factor and the RMS delay spread for all three frequency bands is given in Tab. II. Additionally, we tabulated the specified correlation coefficient for the urban micro scenario from 3rd Generation Partnership Project (3GPP) [25]. We conclude that the estimated correlation coefficient is close to the value specified in 3GPP [25]. We observe that the correlation coefficient is negative, frequency dependent, and its magnitude increases with carrier frequency. We emphasize that the used antennas have approximately equal directivity and variation in correlation coefficient is not explainable by different directivity of the antennas.

TABLE II
ESTIMATED PARAMETERS FROM MEASUREMENTS AND 3GPP [25]

Freq. Band	K-factor [dB]		σ_τ [ns]		ρ	
	Estimated					3GPP
	Mean	Std.	Mean	Std.		
3.2 GHz	4.93	3.98	123.66	49.87	−0.498	−0.7
34.3 GHz	5.49	4.25	119.63	49.05	−0.703	−0.7
62.35 GHz	4.52	4.48	131.48	49.46	−0.769	−0.7

V. CONCLUSION

We analyze the time-varying Rician K-factor from V2I multi-band channel measurements with a moving transmitter. Specifically, the measurements are conducted simultaneously at center frequencies of 3.2 GHz, 34.3 GHz and 62.35 GHz, using antennas with comparable radiation patterns. The measured results show that the K-factor is not constant, but varies over time. Furthermore, the results demonstrate only minor differences in the K-factor across different frequency bands, indicating similar propagation conditions at both cmWave and mmWave frequencies. Moreover, the K-factor and RMS delay spread are shown to be inversely related: as the K-factor decreases, the RMS delay spread increases, and vice versa, consistent with existing literature. The correlation coefficient between the K-factor and the RMS delay spread is frequency dependent and its magnitude increases with carrier frequency.

REFERENCES

[1] 3GPP, "Technical Specification Group Radio Access Network; NR; User Equipment (UE) radio transmission and reception; Part 1: Range 1 Standalone," 3rd Generation Partnership Project (3GPP), Technical Specification (TS) 38.101-1, 2022, version 17.5.0.

[2] B. Ai, A. F. Molisch, M. Rupp, and Z. D. Zhong, "5G key technologies for smart railways," *Proceedings of the IEEE*, vol. 108, no. 6, 2020.

[3] F. Pasic, N. Di Cicco, M. Skocaj, M. Tornatore, S. Schwarz, C. F. Mecklenbräuker, and V. Degli-Esposti, "Multi-band measurements for deep learning-based dynamic channel prediction and simulation," *IEEE Communications Magazine*, vol. 61, no. 9, pp. 98–104, 2023.

[4] D. Dupleich, R. Muller, C. Schneider, S. Skoblikov, J. Luo, M. Boban, G. Del Galdo, and R. Thoma, "Multi-band vehicle to vehicle channel measurements from 6 GHz to 60 GHz at "T" intersection," in *2nd Connected and Automated Vehicles Symposium (CAVS)*, 2019.

[5] M. Boban, D. Dupleich, N. Iqbal, J. Luo, C. Schneider, R. Müller, Z. Yu, D. Steer, T. Jämsä, J. Li, and R. S. Thomä, "Multi-band vehicle-to-vehicle channel characterization in the presence of vehicle blockage," *IEEE Access*, vol. 7, pp. 9724–9735, 2019.

[6] M. Hofer, D. Löschenbrand, J. Blumenstein, H. Groll, S. Zelenbaba, B. Rainer, L. Bernadó, J. Vychodil, T. Mikulasek, E. Zöchmann, S. Sangodoyin, H. Hammoud, B. Schrenk, R. Langwieser, S. Pratschner, A. Prokes, A. F. Molisch, C. F. Mecklenbräuker, and T. Zemen, "Wireless vehicular multiband measurements in centimeterwave and millimeterwave bands," in *IEEE 32nd Annual International Symposium on Personal, Indoor and Mobile Radio Communications (PIMRC)*.

[7] M. Hofer, D. Löschenbrand, S. Zelenbaba, A. Dakić, B. Rainer, and T. Zemen, "Wireless 3GHz and 30 GHz vehicle-to-vehicle measurements in an urban street scenario," in *IEEE 96th Vehicular Technology Conference (VTC2022-Fall)*, 2022.

[8] M. Hofer, D. Löschenbrand, F. Pasic, D. Radovic, B. Rainer, J. Blumenstein, C. F. Mecklenbräuker, S. Sangodoyin, H. Hammoud, G. Matz, A. F. Molisch, and T. Zemen, "Similarity of wireless multiband propagation in urban vehicular-to-infrastructure scenarios," in *IEEE 35th Annual International Symposium on Personal, Indoor and Mobile Radio Communications (PIMRC)*, 2024. [Online]. Available: https://thomaszemen.org/papers/Hofer24-PIMRC-paper.pdf

[9] H. Wang, X. Yin, J. Rodríguez-Piñeiro, J. Lee, and M. Kim, "Shadowing and Multipath-Fading Statistics at 2.4 GHz and 39 GHz in Vehicle-to-Vehicle Scenarios," in *2020 14th European Conference on Antennas and Propagation (EuCAP)*, 2020.

[10] C. Ling, H. Chen, C. Li, Q. Qin, and X. Yin, "Characterization of mmWave and sub-6 GHz propagation channels in manufacturing scenarios," in *IEEE Globecom Workshops (GC Wkshps)*, 2023.

[11] F. Pasic, D. Schützenhöfer, E. Jirousek, R. Langwieser, H. Groll, S. Pratschner, S. Caban, S. Schwarz, and M. Rupp, "Comparison of sub 6 GHz and mmWave wireless channel measurements at high speeds," in *16th European Conference on Antennas and Propagation (EuCAP 2022)*, 2022.

[12] F. Pasic, M. Hofer, M. Mussbah, H. Groll, T. Zemen, S. Schwarz, and C. F. Mecklenbräuker, "Statistical evaluation of delay and Doppler spreads in sub-6 GHz and mmWave vehicular channels," in *IEEE 97th Vehicular Technology Conference (VTC2023-Spring)*, 2023.

[13] D. Radovic, F. Pasic, M. Hofer, H. Groll, C. F. Mecklenbräuker, and T. Zemen, "Stationarity evaluation of high-mobility sub-6 GHz and mmWave non-WSSUS channels," in *XXXVth General Assembly and Scientific Symposium of the International Union of Radio Science*, 2023.

[14] H. Miao, J. Zhang, P. Tang, L. Tian, X. Zhao, B. Guo, and G. Liu, "Sub-6 GHz to mmWave for 5G-advanced and beyond: Channel measurements, characteristics and impact on system performance," *IEEE Journal on Selected Areas in Communications*, vol. 41, no. 6, pp. 1945–1960, 2023.

[15] A. F. Molisch, *Wireless communications: From Fundamentals to Beyond 5G*, 3rd ed. IEEE Press - Wiley, 2023.

[16] F. Pasic, M. Hofer, M. Mussbah, S. Caban, S. Schwarz, T. Zemen, and C. F. Mecklenbräuker, "Channel estimation for mmWave MIMO using sub-6 GHz out-of-band information," in *2024 International Conference on Smart Applications, Communications and Networking (SmartNets)*.

[17] L. Bernadó, T. Zemen, F. Tufvesson, A. F. Molisch, and C. F. Mecklenbräuker, "Time- and frequency-varying K-factor of non-stationary vehicular channels for safety-relevant scenarios," *IEEE Transactions on Intelligent Transportation Systems*, vol. 16, no. 2, pp. 1007–1017, 2015.

[18] M. Friese, "Multitone signals with low crest factor," *IEEE Transactions on Communications*, vol. 45, no. 10, pp. 1338–1344, 1997.

[19] D. Löschenbrand, M. Hofer, L. Bernadó, G. Humer, B. Schrenk, S. Zelenbaba, and T. Zemen, "Distributed massive MIMO channel measurements in urban vehicular scenario," in *13th European Conference on Antennas and Propagation (EuCAP)*, 2019.

[20] E. Sousa, V. Jovanovic, and C. Daigneault, "Delay spread measurements for the digital cellular channel in Toronto," *IEEE Transactions on Vehicular Technology*, vol. 43, no. 4, pp. 837–847, 1994.

[21] C. Oestges, N. Czink, B. Bandemer, P. Castiglione, F. Kaltenberger, and A. J. Paulraj, "Experimental characterization and modeling of outdoor-to-indoor and indoor-to-indoor distributed channels," *IEEE Transactions on Vehicular Technology*, vol. 59, no. 5, pp. 2253–2265, 2010.

[22] L. Greenstein, D. Michelson, and V. Erceg, "Moment-method estimation of the Ricean K-factor," *IEEE Communications Letters*, vol. 3, no. 6, pp. 175–176, 1999.

[23] L. Bernadó, T. Zemen, F. Tufvesson, A. F. Molisch, and C. F. Mecklenbräuker, "Delay and Doppler spreads of nonstationary vehicular channels for safety-relevant scenarios," *IEEE Transactions on Vehicular Technology*, vol. 63, no. 1, 2014.

[24] D. Slepian, "Prolate spheroidal wave functions, fourier analysis, and uncertainty — v: the discrete case," *The Bell System Technical Journal*, vol. 57, no. 5, pp. 1371–1430, 1978.

[25] 3GPP, "Study on channel model for frequencies from 0.5 to 100 GHz," 3rd Generation Partnership Project (3GPP), Technical report (TR) 38.901, 2022, version 17.0.0.